Journal of Solid State Chemistry **147,** 185–198 (1999)
Article ID jssc.1999.8212, available online at http://www.idealibrary.com on IDEAL®

Giant Magnetoresistance in $CaCu_3Mn_4O_{12}$-Based Oxides with Perovskite-Type Structure

Z. Zeng,* M. Greenblatt,*,[1] J. E. Sunstrom IV,* and M. Croft†

*Department of Chemistry and †Department of Physics, Rutgers, The State University of New Jersey, Piscataway, NJ 08855

and

S. Khalid

Brookhaven National Laboratory, 725 D, Upton, New York 11973

Received November 17, 1998; in revised form January 26, 1999; accepted January 27, 1999

$Ca_{0.5}Na_{0.5}Cu_{2.5}Mn_{4.5}O_{12}$, $CaCu_{3-x}Mn_{4+x}O_{12}$ ($0.5 \le x \le 2$) were prepared at 700°C and 2600 PSI by combined sol–gel and high oxygen pressure methods. $CaCu_{0.5}Mn_{6.5}O_{12}$ and $CaMn_7O_{12}$ ($x=2.5$ and 3) were prepared by solid state reactions in evacuated quartz tubes at 900°C. These compounds crystallize in a body-centered cubic variant of the perovskite structure except for $CaMn_7O_{12}$, which has rhombohedral symmetry. The oxidation states of Cu and Mn were investigated by X-ray absorption spectroscopy and chemical analysis. The oxidation state of Mn is near 4+ in $Ca_{0.5}Na_{0.5}Cu_{2.5}Mn_{4.5}O_{12}$ and decreases with increasing x. $Ca_{0.5}Na_{0.5}Cu_{2.5}Mn_{4.5}O_{12}$, $CaCu_{2.5}Mn_{4.5}O_{12}$ ($x=0.5$), and $CaCu_{1.5}Mn_{5.5}O_{12}$ ($x=1.5$) undergo a semiconductor-to-metal transition (T_{SM}), $CaCu_2Mn_5O_{12}$ ($x=1.0$) is metallic, while the $2.0 \le x \le 3.0$ phases are semiconducting in the range 10–400 K. All of the materials (except the $x=2.5$ and 3.0) undergo a paramagnetic-to-ferromagnetic-like transition below their ordering temperatures (T_C). The $CaCu_{0.5}Mn_{6.5}O_{12}$ and $CaMn_7O_{12}$ ($x=2.5$ and 3.0) materials order antiferromagnetically at (T_N) 40 and 20 K, respectively. The magnetic and resistivity results are summarized in a T–x phase diagram. The ordering temperatures decrease with increasing Mn^{3+} content, hence the double exchange mechanism does not appear to govern the ferromagnetic ordering. The highest magnetoresistance reaches a maximum of −32% for $Ca_{0.5}Na_{0.5}Cu_{2.5}Mn_{4.5}O_{12}$ and is −28% for $CaCu_{2.5}Mn_{4.5}O_{12}$ at 4.2 K and 5 T. In general, the magnetoresistance does not occur at the semiconductor-to-metal transition and it decreases smoothly with increasing temperature or x. These materials show high sensitivity of the magnetoresistance at low applied magnetic fields and good temperature stability of the magnetoresistance. © 1999 Academic Press

[1]To whom correspondence should be addressed. Tel.: E-mail: martha@rutchem.rutgers.edu.

INTRODUCTION

In 1993, giant magnetoresistance (GMR) effects were reported in $La_{1-x}Ca_xMnO_3$ films (1, 2). This finding has led to renewed interest in perovskite-related oxides, particularly the rare earth manganates, $LnMnO_3$, and substituted analogs $La_{1-x}A_xMnO_3$ (A = alkaline earth or alkali metal) (3–6), because of their potential technological applications for magnetic memory, sensor, and actuator devices. Recently, other systems including $La_{1-x}A_xCoO_3$ (7, 8), Cr-based chalcogenides (9), and $Tl_2Mn_2O_7$ (10, 11) were also reported with a large negative magnetoresistance (MR) effect, although the structure of these materials (with the exception of the Co phases) are different from that of the perovskite. A common property of these materials is a semiconductor (insulator)-to-metal transition (T_{SM}) near a paramagnetic-to-ferromagnetic transition, the Curie temperature (T_C). In an applied magnetic field **H**, usually several teslas (T), the resistivity of the sample greatly decreases, i.e., the so-called magnetoresistance (MR) effect. MR for a given temperature is defined by the relationship: $MR = (\rho_H - \rho_0)/\rho_0$, where ρ_H and ρ_0 are the resistivity in an applied magnetic field of **H** or zero, respectively. In general MR is highest, near the T_{IM}. The MR increases with H and may not be saturated even at 6 T.

These properties are different from those observed in multilayer-metal GMR materials (12–18), which do not have a semiconductor-to-metal transition and where the MR smoothly increases with decreasing temperature. Therefore, these new oxides are now generally referred to as colossal magnetoresistance (CMR) materials, not only because they have very large MRs, but also because of their different chemical and physical properties from those of the conventional GMR materials.

0022-4596/99 $30.00
Copyright © 1999 by Academic Press
All rights of reproduction in any form reserved.

Although the MRs of the CMR manganates are very large ($\sim$100%), major technical problems must be solved before their practical application can be realized: for example, the manganates have high MRs only at high fields (several T); at low fields and at room temperature (RT) the response is negligible. Much effort has been made to improve the MR response at low fields (19, 20); nevertheless, the MR of the manganates at low fields is significantly lower than that of the more conventional GMR materials at RT. New materials with high MR at low fields are needed to improve the magnetic signal of current computer disks. Further, the MR effect of the manganates is related to the semiconductor-to-metal transition, which typically manifests itself as a sharp peak in the resistivity versus temperature (ρ–T) response; thus the MR also changes rapidly near T_{SM}. Therefore, the temperature range for a stable, high MR is narrow. However, for practical applications, significant temperature stability is required. Finally, the largest MRs often occur well below RT, which is another disadvantage for practical device applications.

$CaCu_3Mn_4O_{12}$ was first reported by Chenavas *et al.* (21). This compound represents an $AA'_3B_4O_{12}$ perovskite-like phase (see Fig. 1a): A is generally a large monovalent or divalent or rare earth cation; A' is Cu^{2+} or Mn^{3+}; and B can be $Mn^{4+/3+}$, Ti^{4+}, Ru^{4+}, or Ge^{4+} (21, 22). The crystal symmetry is cubic (space group $Im3$) with a doubling of the ideal ABO_3 perovskite cell. The doubling of the unit cell is due to the ordering of the A and A' ions and the distortion of the oxygen sublattice, which leads to a tilted three-dimensional network of BO_6 octahedra sharing corners (23). The B–O–B angle is $\sim$142° instead of 180°, as in the ideal perovskite structure. This distortion creates two different polyhedra at the A/A' site: a slightly distorted 12 oxygen-coordinated A' site and a grossly distorted icosahedron at the A' site. There are three sets of A'–O distances at $\sim$1.9, 2.8, and 3.2 Å each forming an approximately square-planar coordination (23). These features of the structure are illustrated in Fig. 1b and c.

One of the unusual characteristics of this structure is that it requires a Jahn–Teller distorted ion, such as Cu^{2+}, at the A' site. Cu^{2+} can be partially or completely substituted by Mn^{3+} (d^4, another Jahn–Teller ion) in the $CaCu_{3-x}Mn_{4+x}O_{12}$ system. Any Mn^{4+} present occupies the B site only. In $YCu_{2.3}Mn_{4.7}O_{12}$, Bochu *et al.* (22) found that the coupling of Mn^{3+}–Mn^{4+} in the Mn–O_2 layer is ferromagnetic, while that of Cu^{2+}–Mn^{4+} on the A' and B sites is antiferromagnetic. This case is somewhat similar to the magnetic interactions in multilayer-metal GMR materials with an alternating ferromagnetic in-layer and antiferromagnetic inter-layer arrangement.

All CMR materials investigated thus far have only one type of magnetic ion, and their properties are governed by double exchange as in Mn^{3+}–O–Mn^{4+} and Co^{3+}–O–Co^{4+}, or super exchange as in Mn^{4+}–O–Mn^{4+} and

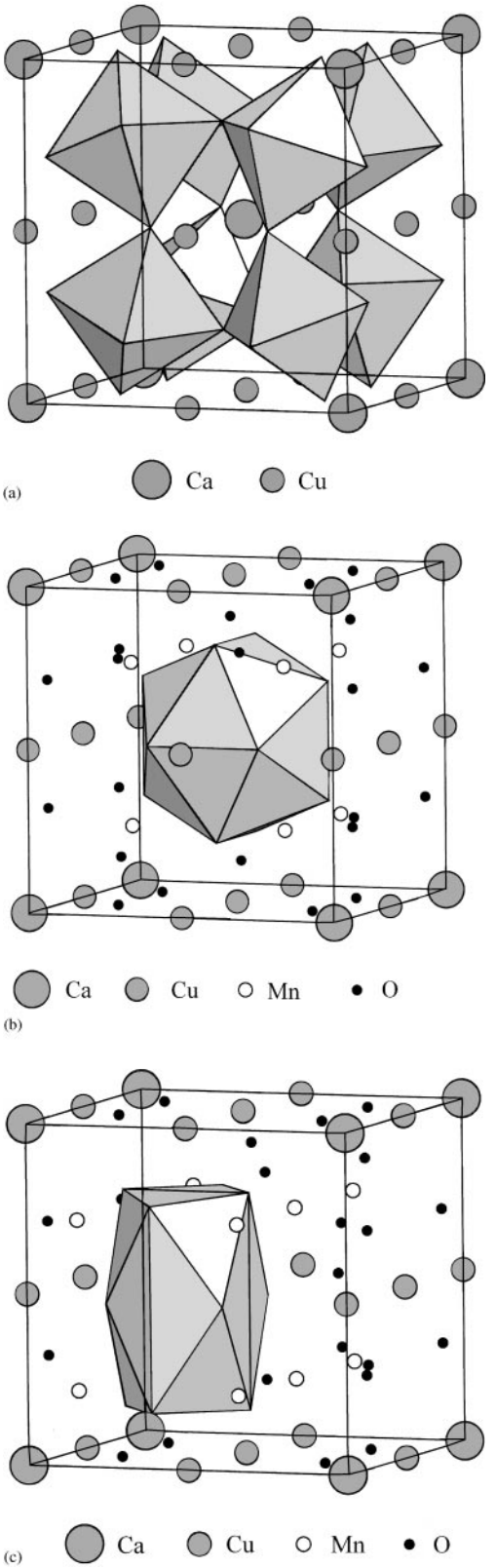

FIG. 1. Structure of $CaCu_3Mn_4O_{12}$ indicating (a) the MnO_6 polyhedral structure; (b) the cubooctahedral AO_{12} polyhedra; and (c) the 12-coordinated polyhedra around the A' (Cu^{2+}/Mn^{3+}) cation.

Mn^{3+}–O–Mn^{3+}. In the $CaCu_{3-x}Mn_xMn_4O_{12}$ system the competing exchange between the magnetic A' site Cu^{2+}/Mn^{3+} and B-site $Mn^{3+/4+}$ ions may lead to interesting behavior including high MR. Moreover, appropriate chemical substitutions in the cation sites and/or alteration of the oxygen content may allow fine-tuning of the electronic and magnetic properties of this system.

$CaCu_3Mn_4O_{12}$ decomposes at about 800°C under ambient pressure and can be stabilized only at 50 kbar pressure (22). The sol–gel technique is a well-known method for the preparation of materials at low temperature; the small particle sizes obtained by this technique enhance particle contact and facilitate reaction. In this paper we report the synthesis of $Ca_{0.5}Na_{0.5}Cu_{2.5}Mn_{4.5}O_{12}$ and $CaCu_{3-x}Mn_{4+x}O_{12}$ ($0.5 \leq x \leq 3$) and the characterization of their electronic, magnetic and MR properties.

EXPERIMENTAL

$Ca_{0.5}Na_{0.5}Cu_{2.5}Mn_{4.5}O_{12}$, $CaCu_{3-x}Mn_{4+x}O_{12}$ ($0.5 \leq x \leq 2$) were prepared by dissolving stoichiometric amounts of $CaCO_3$ (99 + % Aldrich), CuO (99.9%, Aldrich), $Mn(NO_3)_2$ (49.7%w/w aqueous solution, Aldrich; concentration was determined by titration), and Na_2CO_3 ((99 + %, Aldrich) in an excess amount of 35% nitric acid; an excess amount of citric acid (99.8% Aldrich), ethylene glycol (99 + %, Aldrich), and ethylenediamine (99 + % Aldrich) were added until the solution was basic, as tested by litmus paper. The solution was slowly evaporated to a resin and dried. The sample was then heated slowly to 600°C to decompose the organic compounds and then pressed into a pellet at 1 kbar. The pellet was wrapped in a piece of gold foil, placed into a high-pressure vessel, and sintered at 700°C, and 0.18 kbar (2600 Psi) of oxygen pressure for 3 days with one intermediate grinding. Finally the sample was slowly cooled down to room temperature under 0.18 kbar oxygen pressure. The high oxygen pressure is required to prevent the decomposition of the desired phase. When the compounds are prepared at ambient pressure, a substantial amount of CuO is found in the powder X-ray diffraction (PXD) pattern, because Mn^{4+} is reduced to Mn^{3+}, which enters the A' site and ejects an equivalent amount of copper. $CaCu_{0.5}Mn_{6.5}O_{12}$ and $CaMn_7O_{12}$ with high Mn^{3+} contents were prepared from stoichiometric amounts of CaO, CuO, MnO_2, and Mn_2O_3, which were mixed and pressed into pellets. The pellets were sealed in evacuated quartz tubes and sintered at 900°C for 3 days.

The PXD data were collected with a SCINTAG PAD V diffractometer with monochromatized Cu$K\alpha$ radiation. Silicon powder was used as an internal standard. Lattice parameters were refined by a least-squares method. The dc electrical resistivity and MR measurements were carried out by a standard four-probe technique and were measured together with the susceptibility from 4 to 400 K in a SQUID magnetometer (MPMS, Quantum Design).

The Mn and Cu K-edge X-ray absorption spectroscopy (XAS) measurements were performed on beam lines X-19A and X-18B at the Brookhaven National Synchrotron Light Source using double crystal Si (311) and channel-cut Si (111) monochromators, respectively. Electron yield, fluorescence mode, and transmission mode measurements were made and checked for consistency. A standard was run simultaneously with all the measurements for precise calibration. The relative energies between various spectra were established by careful comparison of the standard spectra. Particular care was taken to use an identical standard sample, which was maintained in a constant position to accurately calibrate the chemical shift results. In general, the relative accuracy of the energy is about ± 0.05 eV. All spectra were normalized to unity step in the absorption coefficient from well below to well above the edge.

Chemical analyses were made with a Baird Atomic Model 2070 inductively coupled plasma emission spectrometer (ICP). The oxidation state of Mn was determined by chemical titration: the samples were dissolved with an excess of $Fe(NH_4)_2(SO_4)_2$ in dilute sulfuric and phosphoric acid and titrated with $KMnO_4$ solution.

RESULTS AND DISCUSSION

Synthesis

Initial attempts to prepare pure $CaCu_3Mn_4O_{12}$ under various conditions yielded the desired phase contaminated with traces of CuO, even at 2600 PSI oxygen pressure (the maximum pressure available). The stoichiometric composition $CaCu_{2.5}Mn_{4.5}O_{12}$, on the other hand, yielded an X-ray pure compound under the available conditions of synthesis. This composition corresponds formally to $Ca(Cu_{2.5}Mn^{3+}_{0.5})(Mn^{3+}_{0.5}Mn^{4+}_{3.5})O_{12}$ (i.e., $AA'_3B_4O_{12}$). Moreover, by partially substituting Na^+ for Ca^{2+}, the formal oxidation state of all of the Mn at the B site can be made to be $4+$ $[(Ca_{0.5}Na_{0.5})(Cu_{2.5}Mn^{3+}_{0.5})(Mn^{4+}_4)O_{12}]$. Single phases of $Ca_{0.5}Na_{0.5}Cu_{2.5}Mn_{4.5}O_{12}$, $CaCu_{3-x}Mn_{4+x}O_{12}$ ($0.5 \leq x \leq 3$) were prepared at low temperatures (700–900°C) and relatively low pressures [≤ 0.18 kbar compared to the 50 Kbar previously used for the preparation of $CaCu_3Mn_4O_{12}$ (21, 22)]. ICP analysis shows excellent agreement, within the experimental error (1–2%), between the expected and observed values of the constituent elements in the final products (Table 1). The relatively large deviation between the observed and calculated values of the oxidation state of Mn in Table 1, particularly for the two compounds with the highest Mn^{4+} content may be an indication of small oxygen nonstoichiometry.

TABLE 1
Element Analysis and the Lattice Parameters of Ca–Cu–Mn–O Compounds

Composition	Ca (wt%)	Cu (wt%)	Mn (wt%)	Oxidation state of Mn	a (Å)
$Ca_{0.5}Na_{0.5}Cu_{2.5}Mn_{4.5}O_{12}$					
Observed	3.15	26.0	39.0	3.84	7.2461(1)
Calculated	3.18	25.2	39.3	3.89	
$CaCu_{2.5}Mn_{4.5}O_{12}$					
Observed	6.19	25.5	38.7	3.68	7.2287(1)
Calculated	6.28	24.9	38.7	3.78	
$CaCu_2Mn_5O_{12}$					
Observed	6.37	20.0	43.3	3.61	7.2652(2)
Calculated	6.32	20.1	43.3	3.60	
$CaCu_{1.5}Mn_{5.5}O_{12}$					
Observed	6.46	15.2	47.9	3.46	7.2816(5)
Calculated	6.37	15.1	48.0	3.45	
$CaCuMn_6O_{12}$					
Observed	6.32	10.5	52.1	3.31	7.3198(6)
Calculated	6.41	10.2	52.7	3.33	
$CaCu_{0.5}Mn_{6.5}O_{12}$					
Observed	6.49	5.01	56.4	3.22	7.3259(6)
Calculated	6.45	5.12	57.5	3.23	
$CaMn_7O_{12}$					
Observed	6.48	0	62.50	3.15	Rhom.
Calculated	6.50	0	62.36	3.14	$a = 6.4024(9)$ $\alpha = 109.686(1)$

Valence of Mn and Cu

$CaCu_{2.34}Mn_{4.66}O_{12}$ has been prepared previously by a hydrothermal method (21, 22) for which the distribution of formal valences was given by the formula $[Ca^{2+}(Cu^{2+}_{0.78}Mn^{3+}_{0.22})_3](Mn^{4+}_{0.835}Mn^{3+}_{0.165})_4O_{12}$. Similarly, the formal valence distribution of the samples prepared here can be described as $[Ca^{2+}_{0.5}Na^{+}_{0.5}(Cu^{2+}_{2.5}Mn^{3+}_{0.5})](Mn^{4+})_4O_{12}$ and $[Ca^{2+}(Cu^{2+}_{3-x}Mn^{3+}_{x})](Mn^{4+}_{4-x}Mn^{3+}_{x})O_{12}$ $(0.5 \le x \le 3)$. Thus while in $La_{1-x}A_xMnO_3$, $Mn^{3+/4+}$ are statistically distributed only on the B site, in the Ca–Cu–Mn–O phase, Mn^{3+} can be located both on the A' and B sites.

The valences of Cu and Mn were investigated by XAS. In Fig. 2 (top) the Cu-K edges of a series of standard Cu-compounds with varying formal valence states are shown. The Cu^+, Cu_2O spectrum is strongly shifted to lower energy relative to the Cu^{2+}, CuO and $Cu^{2.15+}$, $La_{1.85}Sr_{0.15}CuO_4$ spectra. The latter two spectra emphasize the variability of the first shoulder/peak feature (in the 8984 to 8986 eV range) for Cu compounds of nearly the same formal valences. To circumvent this ambiguity the chemical shift of these Cu compounds will be defined here by the energy that the spectrum first crosses, the absorption coefficient $\mu = 0.8$ value (with $\mu = 1.0$ being normalized to the continuum step across the edge at about 150 eV above the edge).

Figure 2 (bottom) shows the Cu-K edges of $Ca_{0.5}Na_{0.5}Cu_{2.5}Mn_{4.5}O_{12}$, $CaCu_{2.5}Mn_{4.5}O_{12}$, $CaCu_2Mn_5O_{12}$, and the $La_{1.85}Sr_{0.15}CuO_4$ standard. Comparison of the $Ca_{0.5}Na_{0.5}Cu_{2.5}Mn_{4.5}O_{12}$ and $CaCu_{2.5}Mn_{4.5}O_{12}$ spectra shows a broadening/intensity loss of the feature near 8986 eV and a clear modification of the spectral features near the absorption peak (centered about 8996 eV). Comparison of the $CaCu_{2.5}Mn_{4.5}O_{12}$ and $CaCu_2Mn_5O_{12}$,

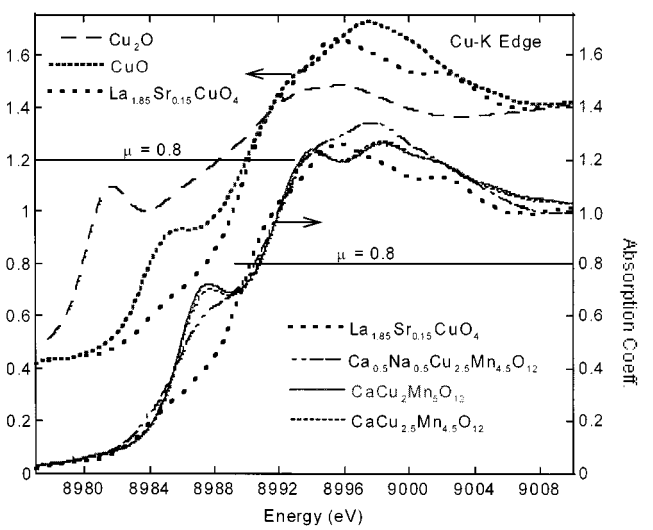

FIG. 2. Cu-K edge spectra for Cu_2O, CuO, and $La_{0.185}Sr_{0.15}CuO_4$ standards and for $Ca_{0.5}Na_{0.5}Cu_{2.5}Mn_{4.5}O_{12}$ and $CaCu_{3-x}Mn_{4+x}O_{12}$ ($x = 0.5$ and 1.0).

spectra, on the other hand shows only small spectral changes. The shifts of the $CaCu_{2.5}Mn_{4.5}O_{12}$ and $CaCu_2Mn_5O_{12}$ spectra (at $\mu = 0.8$) are the same and that of the $Ca_{0.5}Na_{0.5}Cu_{2.5}Mn_{4.5}O_{12}$ spectrum is slightly downshifted. Despite the uncertainties presented by the various near-edge feature variations, the shifts of all of the spectra lie in the vicinity of that expected for a formally Cu^{2+} valence state assignment for these perovskite-related compounds.

Figure 3a (top) shows the Mn-K edges of a series of standard Mn compounds with varying formal valences: Mn^{3+} in $LaMnO_3$; and Mn^{4+} in $CaMnO_3$ and MnO_2. The position of the leading edge of the $CaMnO_3$ spectrum, midway between the two-step rise of the MnO_2 spectrum, again emphasizes the variability of near-edge structure in materials with formally equivalent valences. As before, the compromise choice of the energy of the $\mu = 0.8$ point as the chemical shift (where the two Mn^{4+} standard spectra cross) is made.

Figure 3a (bottom) shows the Mn-K edges of the $Ca_{0.5}Na_{0.5}Cu_{2.5}Mn_{4.5}O_{12}$ and $CaCu_{3-x}Mn_{4+x}O_{12}$ ($0.5 \leq x \leq 3$) compounds, along with that of the $CaMnO_3$ as a standard. It should be noted that there are strong, systematic changes between these spectra in the ranges identified in the figure as the *A* and *B* features (these features are associated with $1s \rightarrow 4p$ excitations. Note that these feature identifications are conventional and the ambiguity with the structure site identifications, although regrettable, is unavoidable. Extra care has been taken to make the identifications clear). Comparison of the $CaCu_{2.5}Mn_{4.5}O_{12}$ and $Ca_{0.5}Na_{0.5}Cu_{2.5}Mn_{4.5}O_{12}$ spectra reveals, for the latter, a strong decrease in *A* feature intensity, a strong energy up-shift in the *B* feature position, and a discernible energy up-shift in the $\mu = 0.8$ position. All of these changes support a strong Mn-*d* character to the Na-doped holes or equivalently, an increased Mn-valence upon Na-substitution, as proposed in the charge description mentioned earlier in this paper.

Comparison of the $CaCu_{3-x}Mn_{4+x}O_{12}$ spectra in Fig. 3a, with increasing *x* (0.5, 1.0, 3.0) reveals: a substantial *A* feature enhancement; an energy down-shift in the $\mu = 0.8$ energy; a broadening of the *B* feature; and a down-shift in the *B* feature peak. These changes are consistent with the proposed substitution of Mn^{3+} onto the Cu^{2+}–*A*′ sublattice accompanied by the partial reduction of the Mn^{4+}–*B*-sublattice to Mn^{3+}. The robust *A* feature in the $x = 3.0$ spectrum is most probably associated with the Mn^{3+} ions on the strongly distorted *A*′ sites. At this site, the oxygen coordination is nearly square planar at 1.9 Å with substantially more distant oxygens apical to this plane (2.8 and 3.2 Å). In general such an *A* feature, associated with transitions into the 4*p* states perpendicular to the square plane, is expected for transition metals in such environments (24).

Figure 3b shows a view of the spectra from Fig. 3a, which is expanded around the $\mu = 0.8$ arbitrarily defined chemical

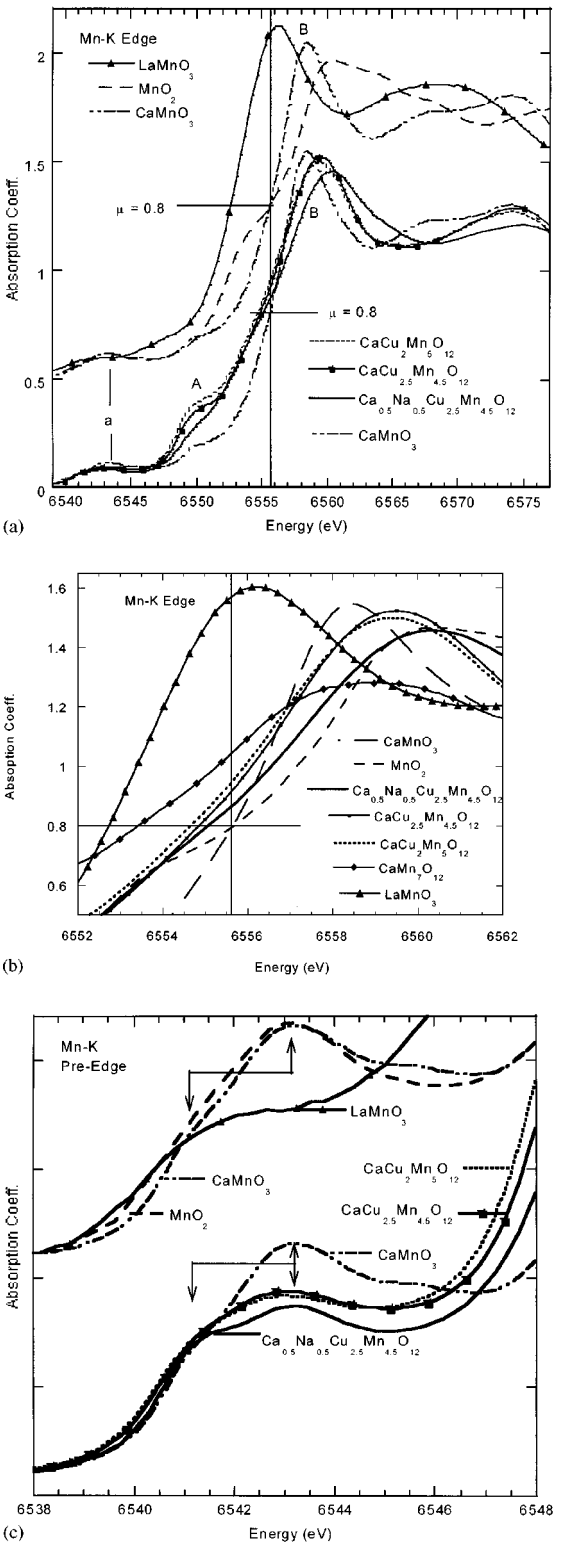

FIG. 3. (a) Mn-K edge spectra for (top) the standards $LaMnO_3$, MnO_2, and (bottom) $CaMnO_3$, $Ca_{0.5}Na_{0.5}Cu_{2.5}Mn_{4.5}O_{12}$, and $CaCu_{3-x}Mn_{4+x}O_{12}$ ($0.5 \leq x \leq 3.0$); (b) An expanded view of the $\mu = 0.8$ chemical shift region for the spectra from the bottom part of the previous figure. (c) An expanded view of the Mn-K pre-edge *a*-feature region for the compounds shown in (a).

shift region. This figure emphasizes the systematic chemical shift to lower energy and underscores the increasing Mn^{3+} content with increasing x in these $CaCu_{3-x}Mn_{4+x}O_{12}$ materials.

Figure 3c (top) shows an expanded view of the Mn-K pre-edge *a*-features of the standard compounds from Fig. 3a. This *a*-feature is ascribed to transitions from the 1*s* core to hybridized *d*/*p* final states (25, 26). The *a*-features of the Mn^{4+} standards (MnO_2 and $CaMnO_3$) exhibit a strong peak near 6543 eV with an unresolved shoulder near 6541 eV (see the connected arrows in the figure). Similar bimodal *a*-feature structures have been interpreted in terms of the t_{2g}–e_g splitting of the 3*d* states in some transition oxides (24). The Mn^{3+} standard ($LaMnO_3$) has a broader, less intense *a*-feature in the 6541–6542 eV range. The onset of the $LaMnO_3$ *a*-feature is also shifted down in energy relative to those of the Mn^{4+} compounds.

Figure 3c (bottom) shows the Mn-K pre-edge *a*-features of the $Ca_{0.5}Na_{0.5}Cu_{2.5}Mn_{4.5}O_{12}$ and $CaCu_{3-x}Mn_{4+x}O_{12}$ ($0.5 \le x \le 3$) compounds along with that of the $CaMnO_3$ as a standard. All of these a-features (except the $x = 3$ case) show a prominent bimodal structure with features near 6541 and 6543 eV. The peak near 6543 eV is associated with the *B* sublattice, Mn^{4+}–e_g component of the spectra, while the 6541 eV shoulder contains both *A*′ and *B* sublattice Mn^{3+} components and a *B* sublattice Mn^{4+}–t_{2g} component. Within the lattice-charge distributions assigned in this paper, the $Ca_{0.5}Na_{0.5}Cu_{2.5}Mn_{4.5}O_{12}$ spectrum manifests the sharpest features by virtue of its Mn^{4+} and Mn^{3+} components being segregated onto the *B* and *A*′ sublattices respectively. Similarly, the broadening of the other two spectra is ascribed to the mixed *A*′ and *B* sublattice distribution of the Mn^{3+} ions. In general the intensity at and below 6541 eV increases with the Mn^{3+} content, and therefore with increasing x in the $CaCu_{3-x}Mn_{4+x}O_{12}$ ($0.5 \le x \le 3$) series. Indeed for the $x = 3$ spectrum this leads to a pronounced downshift of the *a*-feature onset. The *A*′ sublattice *a*-feature should have an additional enhancement due to the increased hybridized *p*-final state component as is seen in transition metal pre-edge features in lower symmetry environments (24, 27–29). This also contributes to the downshifted intensity of the $x = 3$ spectrum.

In summary, the Cu-K and Mn-K main-edge and the Mn-K pre-edge XAS results support the proposed formal charge assignments in these compounds: $[Ca^{2+}_{0.5}Na^{+}_{0.5}(Cu^{2+}_{2.5}Mn^{3+}_{0.5})](Mn^{4+})_4O_{12}$ and $[Ca^{2+}(Cu^{2+}_{3-x}Mn^{3+}_{x})](Mn^{4+}_{4-x}Mn^{3+}_{x})O_{12}$.

Crystallographic Properties

$Ca_{0.5}Na_{0.5}Cu_{2.5}Mn_{4.5}O_{12}$ and $CaCu_{3-x}Mn_{4+x}O_{12}$ ($0.5 \le x \le 2.5$) can be indexed with cubic symmetry, in space group *Im*3; $CaMn_7O_{12}$ distorts to rhombohedral symmetry. The refined unit cell parameters are listed in Table 1.

The cell parameters are double of that of the simple ABO_3 perovskite, due to an ordered arrangement of Ca^{2+} and Cu^{2+}/Mn^{3+} ions on the *A* and *A*′ sites. The lattice parameters increase with increasing x. This trend is consistent with the effective ionic radii of Cu^{2+} (0.71 Å), in square planar coordination; Ca^{2+} (1.48 Å) and Na^{+} (1.53 Å) in a 12-coordinated site; and those of Mn^{3+} (0.78 Å HS), and Mn^{4+} (0.67 Å) in octahedral sites (30). Moreover, an increasing Mn^{3+} content of the *A*′ site does not seem to affect the lattice parameters significantly (i.e., one would expect a slight decrease of the lattice parameter with increasing Mn^{3+} and decreasing Cu^{2+} content, Cu^{2+} being larger than Mn^{3+} (21)).

Magnetic Properties

Figures 4a and 4b show the magnetic susceptibility (χ) and inverse susceptibility (χ^{-1}) as a function of temperature for the samples studied. Figure 5 summarizes the magnetic and resistivity measurements (presented below) into a phase diagram for $Ca_{0.5}Na_{0.5}Cu_{2.5}Mn_{4.5}O_{12}$ and $CaCu_{3-x}Mn_{4+x}O_{12}$ ($0.5 \le x \le 3$). With two magnetic lattice sites, two Mn valences and three magnetic species (Cu^{2+} and $Mn^{3+/4+}$) the magnetism in this system is understandably complex. Both ferrimagnetic and noncolinear ferromagnetism have been reported in related systems (22), while Collomb *et al.* (27) concluded that $CaCu_3Mn_4O_{12}$ is ferromagnetic.

The development of a spontaneous FM moment below a Curie temperature is clear for the $0.5 \le x \le 2.0$ systems. The inverse susceptibilities above T_C obey the Curie–Weiss law ($\chi = C/(T - \theta)$) with Weiss constants (θ) which coincides very well with T_C in this x range. It should be noted, however, that the temperature range accessible in these experiments was too limited to search for the χ^{-1} curvature associated with the crossover to a high-temperature AF-like behavior typical of ferrimagnets (31).

There is clearly a very strong x-dependence of the maximum χ (χ_{max}) in the data of Fig. 6a. This indicates that the AF correlations reducing the FM moment must be substantial and variable across the series (see Fig. 6a). Figure 5b shows the magnetization of $Ca_{0.5}Na_{0.5}Cu_{2.5}Mn_{4.5}O_{12}$ as a function of applied magnetic field, at 20 K. The coercive field ($\mathbf{H}_c$) is seen to be about 100 G and the saturation magnetization is 3.89×10^4 emu/mol. Thus the χ_{max} vs x in these soft magnetic materials should reflect the variations of the compensating spins on the various sublattices. For later comparison to the magnetoresistence, Fig. 6c presents a plot of the square of the magnetization and Fig. 6d the magnetoresistance as a function of H.

Substitution of Mn^{3+} for Cu^{2+} depresses the FM transition temperature until a crossover to the AF order occurs for $2 < x < 2.5$. The $CaCu_{0.5}Mn_{6.5}O_{12}$ ($x = 2.5$) and

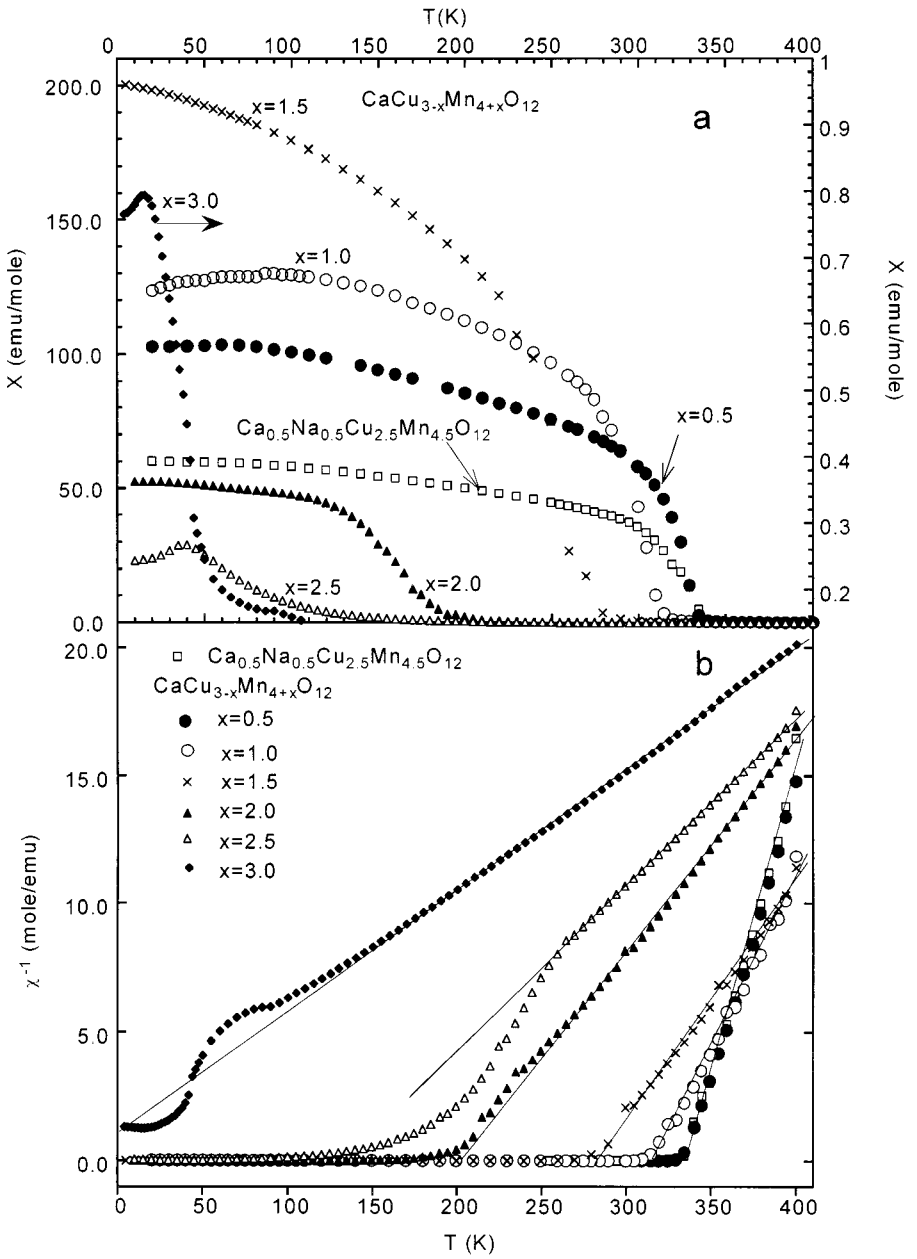

FIG. 4. (a) Magnetic susceptibility as a function of temperature for $Ca_{0.5}Na_{0.5}Cu_{2.5}Mn_{4.5}O_{12}$ and $CaCu_{3-x}Mn_{4+x}O_{12}$ ($0.5 \leq x \leq 3.0$). (b) The inverse of the magnetic susceptibility curves in (a) versus temperature.

$CaMn_7O_{12}$ ($x = 3$) susceptibility curves indicate susceptibility peaks characteristic of AF behavior. The magnetic interactions and phase diagram, in this high x range, are however, not simple. For the $x = 3$ sample, for example, consider the small but distinct cusp in χ near 100 K and the upward deviation in χ^{-1} from C–W behavior near the same temperature. Thus the rapid rise in χ near 40 K and the cusp near 15 K may manifest order rearrangement within a subtle magnetic phase that onset near 100 K.

In the case of the $x = 2.5$ sample the AF-like peak near 50 K is clear. However, close inspection of the χ^{-1} data reveals a strong curvature (away from C–W behavior) in the 200–250 K range. Such a curvature could come from weak ferrimagnetic correlations, so that the short/long-range magnetic order of the $x = 2.5$ sample in the 50–250 K range represents a more subtle and open question.

How the properties of the $Na_{0.5}Ca_{0.5}Cu_{2.5}Mn_{4.5}O_{12}$ material (prepared to drive the B sublattice to full Mn^{4+}) fits

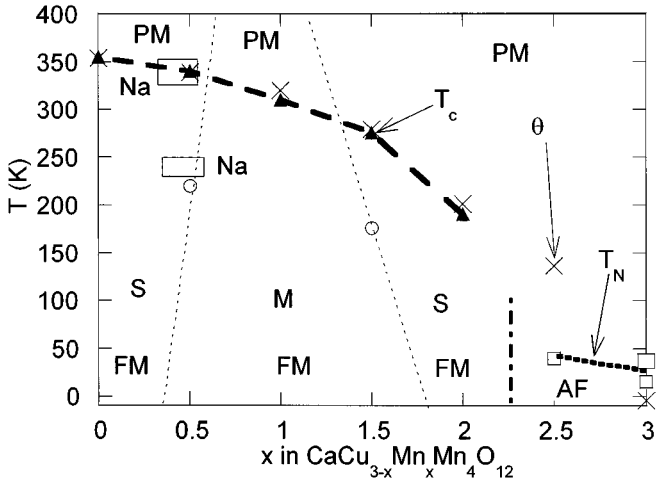

FIG. 5. A summary of the phase diagram for the $Ca_{0.5}Na_{0.5}Cu_{2.5}Mn_{4.5}O_{12}$ and $CaCu_{3-x}Mn_{4+x}O_{12}$ ($0.5 \leq x \leq 3.0$) systems including the paramagnetic (PM), ferromagnetic (or ferrimagnetic, FM), antiferromagnetic (AF), semiconducting (S), and metallic (M) regimes. The PM–FM transition line (heavy long-dashed) connects the FM transition temperature (solid triangles). The AF transition line (heavy short-dashed) connects the AF transition temperatures (open squares: the higher T (larger square) for the $x = 3.0$ sample represents the inflection point in the susceptibility rise, and the lower T (smaller square) represents the susceptibility peak). The heavy dot-dashed line marks the approximate FM-to-AF crossover. The paramagnetic Curie-Weiss θ parameters are plotted as ×'s. A gap has been left in the PM–FM and PM–AF magnetic order line where no measurements were made. The open circle indicates the high-T semiconducting-to-low-T metallic crossover for the $x = 0.5$ and $x = 1.5$ samples and the light dashed line indicates the approximate S-to-M crossover. The boxes indicate the pertinent temperature for the $Ca_{0.5}Na_{0.5}Cu_{2.5}Mn_{4.5}O_{12}$ material.

into this series is of course and important question here. In terms of the FM T_C this material is comparable to the $x = 0.5$ of the $CaCu_{3-x}Mn_{4+x}O_{12}$ system; however, the insensitivity of T_C to x (and the Mn^{4+} content) in this range is not surprising. In terms of the maximum of $\chi(T)$ the Na sample has a lower value than the $x = 0.5$ sample. This is consistent with the Na-induced increase of the Mn^{4+} (as also shown by the XAS results).

Transport Properties

The temperature dependencies of the resistivities of the samples studied are shown from various perspectives in Figs. 7a, b and 8a–c. Qualitative Seebeck measurements for $Ca_{0.5}Na_{0.5}Cu_{2.5}Mn_{4.5}O_{12}$ and $CaCu_{3-x}Mn_{4+x}O_{12}$ show n-type behavior except for $CaMn_7O_{12}$ which is p-type.

The overall resistivity magnitude and thermal variations for the samples studied (see Figs. 7a, b) clearly partition this

TABLE 2
Magnetic Ordering Temperatures, T_C or T_N, Weiss Constants (θ), and Room Temperature resistivities (ρ_{RT}) of $Ca_{0.5}Na_{0.5}Cu_{2.5}Mn_{4.5}O_{12}$, $CaCu_{3-x}Mn_{4+x}O_{12}$

Composition	T_C (K)	T_N (K)	θ (K)	ρ_{RT} (Ω-cm)
$Ca_{0.5}Na_{0.5}Cu_{2.5}Mn_{4.5}O_{12}$	340		+ 347	0.28
$CaCu_{2.5}Mn_{4.5}O_{12}$	340		+ 339	0.054
$CaCu_2Mn_5O_{12}$	310		+ 320	0.0033
$CaCu_{1.5}Mn_{5.5}O_{12}$	275		279	0.16
$CaCuMn_6O_{12}$	190		201	0.2
$CaCu_{0.5}Mn_{6.5}O_{12}$		40	136	4.3
$CaMn_7O_{12}$		15	− 4.4	535

system into $x < 0.5$ semiconducting (S), $0.5 \leq x \leq 1.5$ metallic (M) and $x \geq 2.0$ semiconducting regions. The $x = 0.5$ and $x = 1.5$ samples cross over from high-temperature S to low-temperature M thermal behavior. These S and M regions have been included in the phase diagram in Fig. 5. The slope of the light dashed lines indicate the S-to-M crossover as a function of temperature seen in the $x = 0.5$ and $x = 1.5$ materials (see Fig. 7a). Interestingly the resistivity results for the most metallic $x = 1$ sample (see Fig. 7a) manifests a flattening at high temperature, which may indicate an M-to-S transition somewhere above 400 K. Such a crossover would be consistent with the joining of the dashed lines in the phase diagram to circumscribe the M region. It is worth noting that the temperature dependence of the most metallic $x = 1.0$ sample in the $T < 170$ K range can be described by a Fermi liquid $\rho \approx \rho_0 + AT^2$ behavior with $\rho_0 = 3130\ \Omega$-cm and $A = 12.7\ \mu\Omega$-cm/K^2 (31).

Again it is useful to consider the relation of the $Ca_{0.5}Na_{0.5}Cu_{2.5}Mn_{4.5}O_{12}$ from the perspective of the resistivity results and the phase diagram in Fig. 5. The S–M crossover of the $Ca_{0.5}Na_{0.5}Cu_{2.5}Mn_{4.5}O_{12}$ sample at 210 K is barely higher than that of the $CaCu_{2.5}Mn_{4.5}O_{12}$ ($x = 0.5$) sample. The absolute value of ρ of the Na sample is also somewhat larger than that of the $x = 0.5$ material. The low T upturn in the resistivity of the Na material is presumably due to localization effects in this phase (32). Thus the transport properties of the Na sample appears to be quite similar to the $x = 0.5$ material, despite the increased Mn^{4+} component stabilized on the B site.

Magnetoresistance

The magnetoresistance studies performed here were focused on the $x < 1.0$ samples, where the FM/T_C remains

FIG. 6. (a) The maximum value of the magnetic susceptibility (M_{max}; at all temperatures) for $\mathbf{H} = 0.1$ T, as in Fig. 4a; the box indicates the value for the $Ca_{0.5}Na_{0.5}Cu_{2.5}Mn_{4.5}O_{12}$ material; (b) magnetization (M) as a function of applied magnetic field ($\mathbf{H}$) for $Ca_{0.5}Na_{0.5}Cu_{2.5}Mn_{4.5}O_{12}$ at $T = 20$ K; (c) M^2 versus the applied magnetic field ($\mathbf{H}$) for $Ca_{0.5}Na_{0.5}Cu_{2.5}Mn_{4.5}O_{12}$; (d) the magnetoresistance (MR) versus $\mathbf{H}$ for $Ca_{0.5}Na_{0.5}Cu_{2.5}Mn_{4.5}O_{12}$.

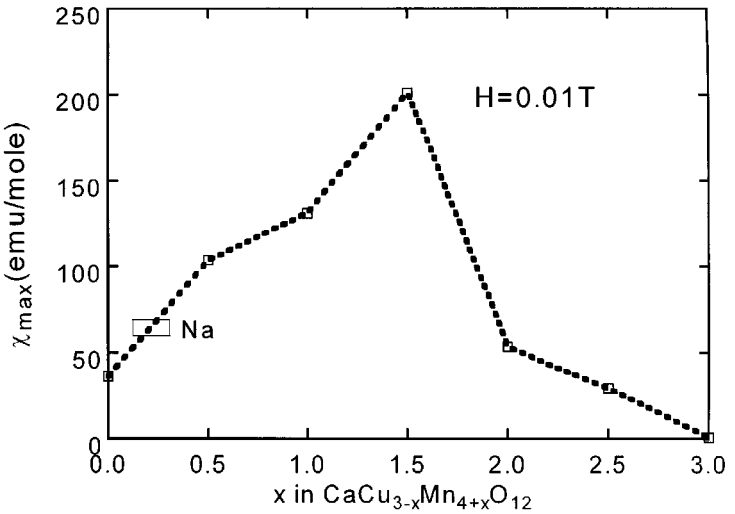
H=0.01T
Na
χ_{max}(emu/mole)
x in $CaCu_{3-x}Mn_{4+x}O_{12}$

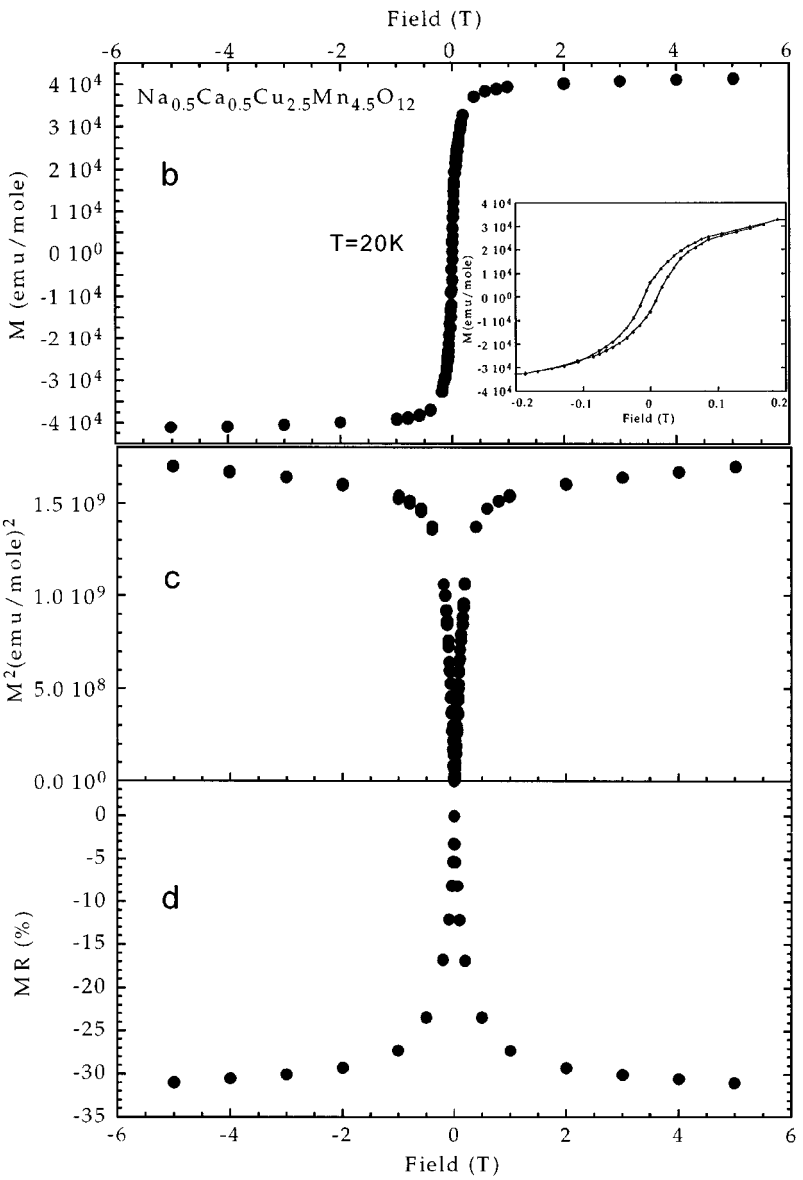
Field (T)
$Na_{0.5}Ca_{0.5}Cu_{2.5}Mn_{4.5}O_{12}$
b
T=20K
M (emu/mole)
c
M^2(emu/mole)^2
d
MR (%)
Field (T)

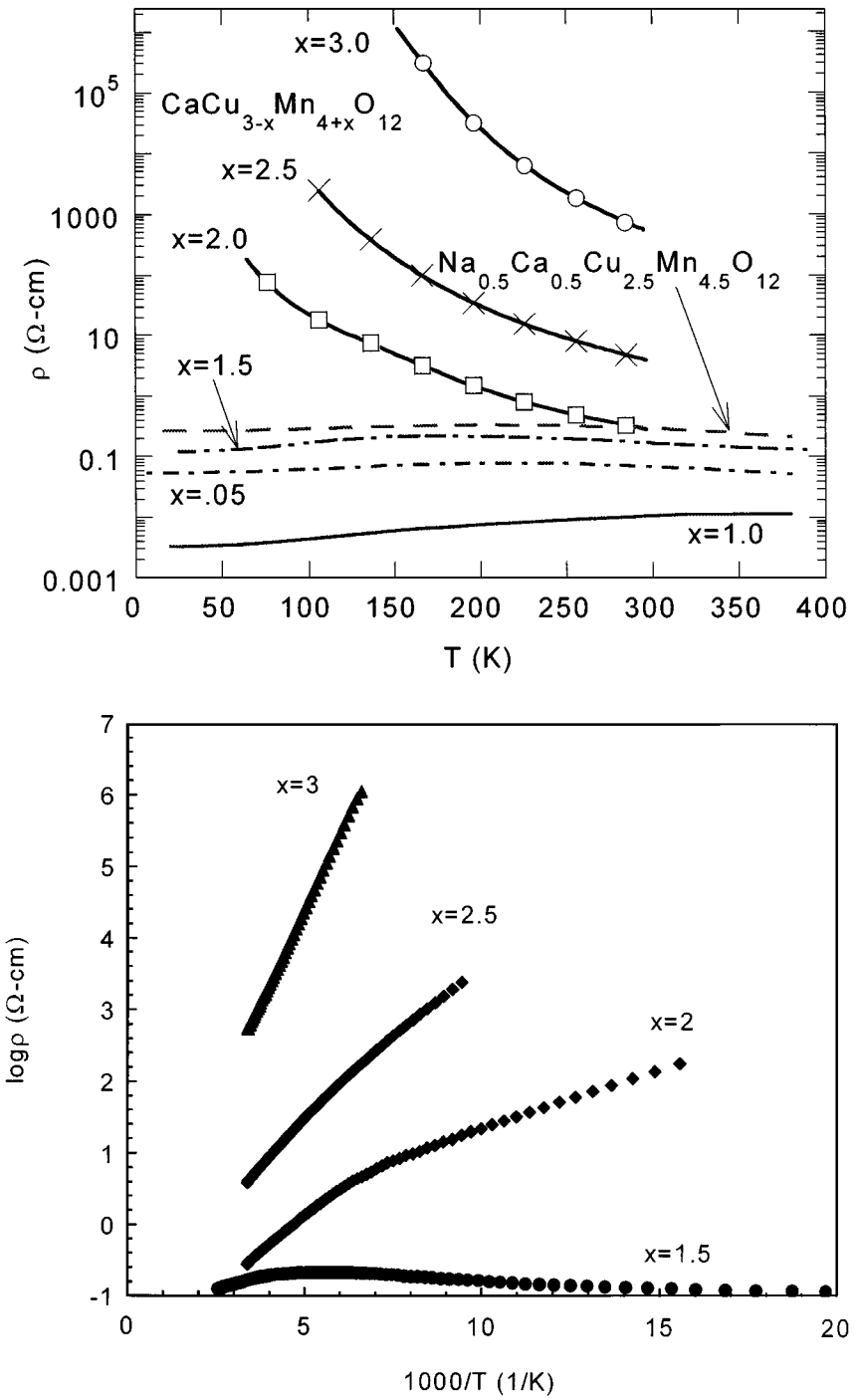

FIG. 7. (a) Resistivity (on a logarithmic scale) as a function of temperature for $CaCu_{3-x}Mn_{4+x}O_{12}$ ($0.5 \leq x \leq 3.0$) and $Ca_{0.5}Na_{0.5}Cu_{2.5}Mn_{4.5}O_{12}$; (b) log ρ vs $1000/T$ for the compounds in Fig. 6a.

sufficiently high to be of technological interest. Specifically, in Figs. 8a–c and 9 the MR of $Ca_{0.5}Na_{0.5}Cu_{2.5}Mn_{4.5}O_{12}$ and $CaCu_{3-x}Mn_{4+x}O_{12}$ ($x = 0.5$ and 1.0) can be seen to be negative and to increase with decreasing temperature. The temperature below, which the MR appears, is quite close to the FM/T_C of the materials. This is consistent with the MR being associated with the spontaneous magnetization. The persistence of some MR just above the T_C could be related to fluctuation effects. Over a substantial temperature range the MR is quasi linear, vanishing near T_C (see Fig. 9). In the mean field theory of the spontaneous magnetization (m), $m \sim (T - T_C)^{1/2}$ near T_C, hence the approximate linearity of

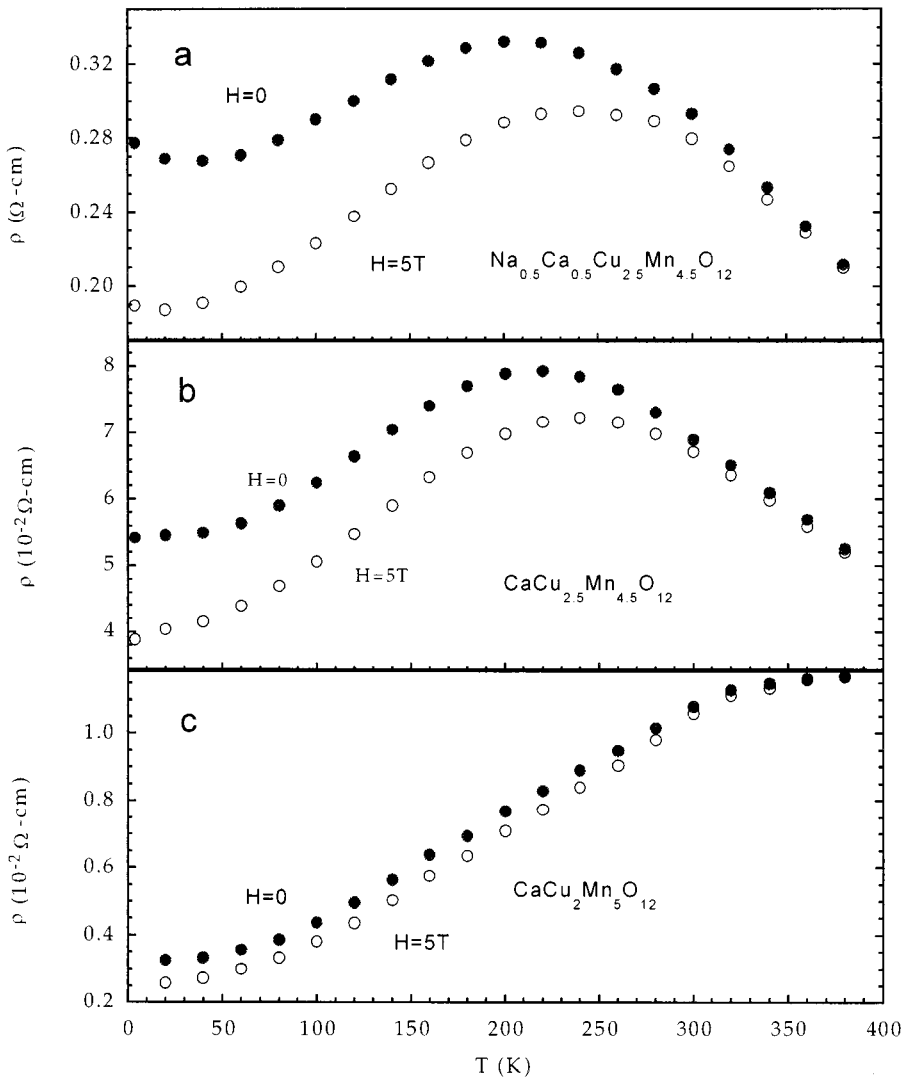

FIG. 8. Resistivity as a function of temperature at $\mathbf{H} = 0$ and $\mathbf{H} = 5$ T for (a) $Ca_{0.5}Na_{0.5}Cu_{2.5}Mn_{4.5}O_{12}$; (b) $CaCu_{2.5}Mn_{4.5}O_{12}$ ($x = 0.5$); and (c) $CaCu_2Mn_5O_{12}$ ($x = 1$).

the MR suggests that, to first order, the MR varies as the spontaneous magnetization squared (i.e., MR $\sim m^2$) (33). Indeed, comparison of the plot of M^2 vs **H** in Fig. 6c to that of MR vs **H** in Fig. 6d reinforces the MR $\sim$m^2 first-order relation.

The low-temperature (< 70 K) resistivity upturn in the Na material was ascribed above to localization effects (32). The $\mathbf{H} = 5$ T resistivity (Fig. 8a) shows a distinct reduction in this upturn, which is consistent with the magnetic field induced remediation of localization. Further, in Fig. 8b and c there appear to be modest enhancements of the MR in the below-70 K range for the $x = 0.5$ and $x = 1.0$ samples also. This is presumably due to the same type of localization effects. In the case of the $x = 1.0$ material there is a discernable break in the thermal variation of MR near TA ≈ 70 K (see Fig. 9). Again this could involve localization effects in this most metallic of these materials. It should be noted that this interpretation would also suggest that the apparent extension of linearity of the MR below 70 K in the Na material and the $x = 0.5$ phase is partially an artifact of localization effects.

The MR is -32% at 20 K and 5 T for $Ca_{0.5}Na_{0.5}Cu_{2.5}Mn_{4.5}O_{12}$. In contrast, for $CaCu_{2.5}Mn_{4.5}O_{12}$ and $CaCu_2Mn_5O_{12}$, with $Mn^{3+/4+}$ present at the *B* site, and the possibility of Mn^{3+}–O–Mn^{4+} double-exchange, the MR is significantly smaller. The Mn^{3+} content on the *B* site increases in the following order: $Ca_{0.5}Na_{0.5}Cu_{2.5}Mn_{4.5}O_{12} < CaCu_{2.5}Mn_{4.5}O_{12} < CaCu_2Mn_5O_{12}$; however, the MR decreases in the same order. Therefore, it seems that the increase of Mn^{3+} content on the *B* site is deleterious for the MR effect. Recall that for the $La_{1-x}A_xMnO_3$ system, the Mn^{3+}–O–Mn^{4+} double exchange mechanism is considered

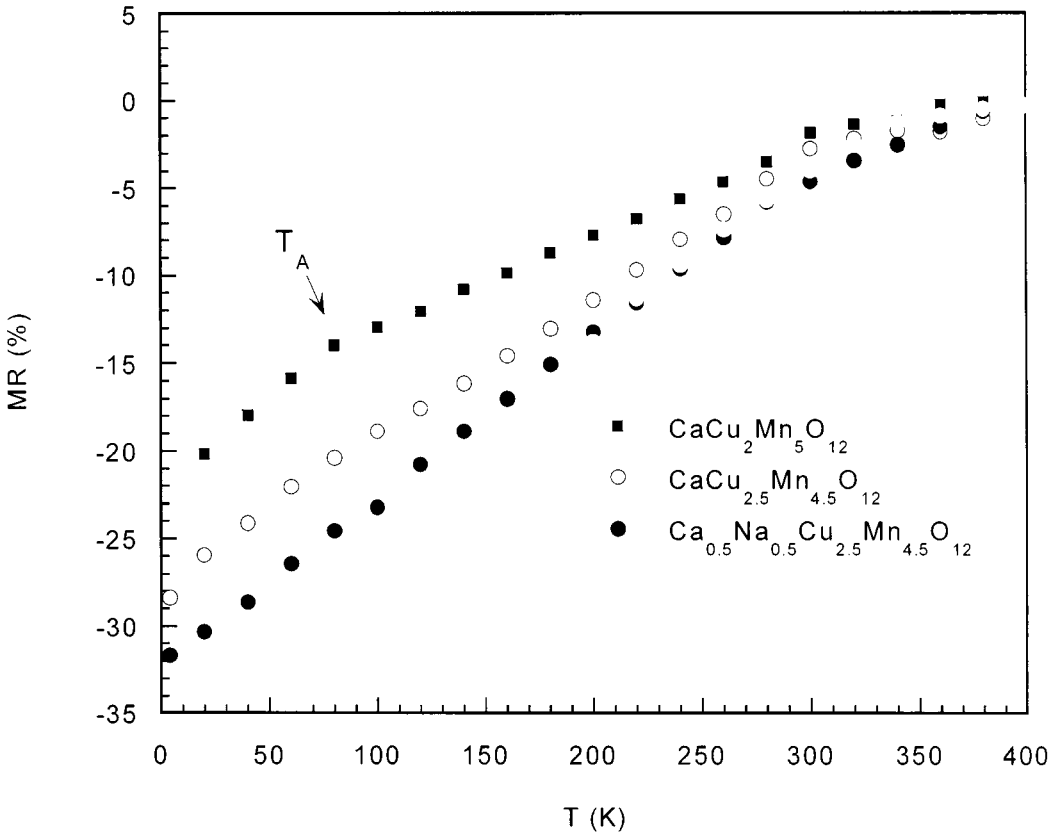

FIG. 9. MR as a function of temperature for $Ca_{0.5}Na_{0.5}Cu_{2.5}Mn_{4.5}O_{12}$, $CaCu_{2.5}Mn_{4.5}O_{12}$, and $CaCu_2Mn_5O_{12}$.

to be important for the MR effect. Thus for the Ca–Cu–Mn–O phases, the Mn^{3+} –O–Mn^{4+} double exchange on the B sites does not appear to govern the observed MR. Indeed, noting that the maximal magnetization is decreasing as the MR is increasing in these materials, it would appear that the AF coupling to the *A* site ions might be crucial in these materials.

$Ca_{0.5}Na_{0.5}Cu_{2.5}Mn_{4.5}O_{12}$ and $Tl_2Mn_2O_7$ have similar properties: (1) probably no Mn^{3+}–O–Mn^{4+} double exchange exists, for the oxidation state of Mn on the *B* site is close to $+4$; (2) the predominant carriers are electrons; (3) the Mn–O–Mn angle is close to 134° for $Tl_2Mn_2O_7$ and 142° for $CaCu_3Mn_4O_{12}$ (11, 21); (4) both show an anomaly in the temperature dependence of resistivity (i.e., an SM for $Ca_{0.5}Na_{0.5}Cu_{2.5}Mn_{4.5}O_{12}$ and a metal-to-metal transition in $Tl_2Mn_2O_7$); 5) in both compounds the spin–charge–lattice couplings do not appear to be especially strong as they are in the rare earth manganates. Further, in $Ca_{0.5}Na_{0.5}Cu_{2.5}Mn_{4.5}O_{12}$, the magnetic couplings are complex: the thus far undetermined Cu^{2+}–O–$Mn^{3+/4+}$ and apparently ferromagnetic Mn^{4+}–O–Mn^{4+} interactions may be responsible for the unusual behavior of this compound.

Figure 6d shows the MR of $Ca_{0.5}Na_{0.5}Cu_{2.5}Mn_{4.5}O_{12}$ as a function of **H** at 20 K. The MR sharply increases at low fields, and almost saturates at ~ 1 T. The MR is 8.2% at 0.05 T. $La_{0.6}Y_{0.07}Ca_{0.33}MnO_3$ was reported to have a CMR, near 100% at high fields (34). However, the MR is only 6.5% at 0.05 T. In other systems, such as $La_{1-x}A_xCoO_3$ (7, 8), Cr-based chalcogenides (9), and $Tl_2Mn_2O_7$ (10, 11), the MR at low field is also very low.

Note the coincidence of the activating field for the MR and the coercive field for the magnetization in Fig. 6c and 6d. From this it is clear: that the high resistivity (at $\mathbf{H} = 0$) is associated with the random orientations of the magnetic domains; and that the high MR is due to the reorientation of this domain structure. The magnitude of the MR, and the (at best) poor conductivity of these materials, support inter-grain/domain tunneling (rather than simple scattering) as the MR mechanism (19, 35). Thus the MR mechanism of spin polarized inter-grain tunneling, along with the small coercive field (~ 100 G) lead to the sharp, low-field response of the MR.

Figure 10 shows a comparison of MR_H/MR_{5T} as a function of **H** in several systems (8, 9, 10, 34) where MR_H and MR_{5T} are the MR at **H** and 5T, respectively. At low fields,

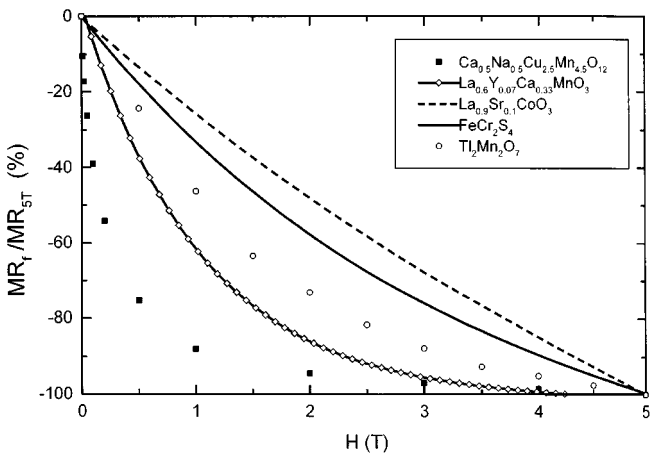

FIG. 10. MR_H/MR_{5T} as a function of **H** for $Ca_{0.5}Na_{0.5}Cu_{2.5}Mn_{4.5}O_{12}$, $La_{0.6}Y_{0.07}Ca_{0.33}MnO_3$, $La_{0.9}Sr_{0.1}CoO_3$, $FeCr_2S_4$, and $Tl_2Mn_2O_7$.

$Ca_{0.5}Na_{0.5}Cu_{2.5}Mn_{4.5}O_{12}$ shows a much sharper response than the other systems, albeit the MR is not very large. This behavior is advantageous for potential device applications. Furthermore, for $La_{1-x}Ca_xMnO_3$, the MR of epitaxially grown films is much larger than that of the bulk materials (2). We are currently working on the growth of Ca–Cu–Mn–O films to optimize the MR properties of this system at low fields, near room temperature.

CONCLUSIONS

Single phase $Ca_{0.5}Na_{0.5}Cu_{2.5}Mn_{4.5}O_{12}$, and $CaCu_{3-x}Mn_{4+x}O_{12}$ $(0.5 \leq x \geq 3.0)$ with a perovskite-related structure were synthesized by combined sol–gel and high oxygen pressure techniques. XAS measurements have been used to probe the complex, but systematic valence state and lattice-site distribution of Mn in these materials. The magnetic and S–M phase diagram for these phases has been determined. $Ca_{0.5}Na_{0.5}Cu_{2.5}Mn_{4.5}O_{12}$ and $CaCu_{3-x}Mn_{4+x}O_{12}$ $(0.5 \leq x \geq 2.0)$ develop a FM moment in the range 340–190 K and exhibit a negative MR at low temperature. In contrast to the substituted $LnMnO_3$ phases T_C does not coincide with T_{SM}, decreases with increasing Mn^{3+} content on the *B* site, the highest MR does not occur at T_{IM}, and the MR increases smoothly with decreasing temperature. Moreover, $Ca_{0.5}Na_{0.5}Cu_{2.5}Mn_{4.5}O_{12}$ with only Mn^{4+} on the *B* site shows the highest MR effect and increasing Mn^{3+} content on the *B* site is deleterious for MR. These results indicate that the Mn^{3+}–O–Mn^{4+} double exchange mechanism used to explain the properties of substituted $LnMnO_3$-type phases may not be operating in these compounds. The dominant MR mechanism in this material appears to be consistent with intergrain tunneling. Finally, $Ca_{0.5}Na_{0.5}Cu_{2.5}Mn_{4.5}O_{12}$ shows a higher sensitivity to **H** at low fields, and better temperature stability than other Mn-perovskite CMR materials. These properties are advantageous for device applications.

ACKNOWLEDGMENTS

The authors thank Dr. I. Fawcett for his help in the X-ray experiments and Professor K. V. Ramanujachary for his suggestions with experimental problems and useful discussions. The ICP analysis was carried out in the Chemistry Department of Rider University with the help of Prof. W. H. McCarroll. We thank Prof. McCarroll for critically reading the manuscript and for his useful suggestions. This work was supported by National Science Foundation-Solid State Chemistry Grants DMR-93-14605 and DMR-96-13106.

REFERENCES

1. K. Chahara, T. Ohno, M. Kasai, and Y. Kozono, *Appl. Phys. Lett.* **63,** 1990. (1993). R. M. Kusters, J. Siug Letou, D. A. Keen, R. McGreeuy, and W. Hayes, *Phys. Rev. B* **155,** 362 (1989). R. Von Helmholt, J. Wecker, B. Holzapfel, L. Schultz, and K. Sanew, *Phys. Rev. Lett.* **71,** 2331 (1993).
2. S. Jin, T. H. Tiefel, M. Mc. Cormack, R. A. Fastnacht, R. Ramesh, and L. H. Chen, *Science* **264,** 413 (1994).
3. A. Urushibara, Y. Moritomo, T. Arima, A. Asamitsu, G. Kido, and Y. Tokura, *Phys. Rev.* B **51,** 14103 (1995).
4. S. Sundar Manoharan, N. Y. Vasanthachaya, M. S. Hegde, K.M. Satyalakshmi, V. Prasad, and S. V. Subramanyam, *J. Appl. Phys.* **76,** 3923 (1994).
5. R. Mahendiran, R. Mahesh, A. K. Raychaudhuri, and C. N. Rao, *J. Phys. D* **28,** 1743 (1995).
6. T. Shimura, T. Hayashi, Y. Inaguma, and M. Itoh, *J Solid State Chem.* **124,** 250 (1996).
7. G. Briceno, H. Chang, X. Sun, P. G. Schultz, and X. D. Xiang, *Science* **270,** 273 (1995).
8. R. Mahendiran, A. K. Raychaudhuri, A. Chainani, and D. D, Sarma, *J. Phys.: Condens. Matter* **7,** L561 (1995).
9. A. P. Ramirez, R. J. Cava, and J. Krajewski, *Nature* **386**, 156 (1997).
10. Y. Shimakuwa, Y. Kubo, and T. Manako, *Nature* **379,** 53 (1996).
11. M. A. Subramanian, B. H. Toby, A. P. Rmirez, W. J. Marshall, A. W. Sleight, and G. H. Kwei, *Science* **273,** 81 (1996).
12. M. N. Baibich, J. M. Broto, A. Fert, F.Nguyen Van Dau, and F. Petroff, *Phys. Rev. Lett.* **61**(21), 2472 (1988).
13. B. Dieny, V. S. Speriosu, S. S. P. Parkin, B. A. Gurner, D. R. Wilhoit, and D. Mauri, *Phys. Rev.* B **43,** 1297 (1991).
14. E. E. Fullerton, M. J. Conover, J. E. Mattson, C. H. Sower, and S. D. Bader, *Appl. Phys. Lett.* **63,** 1699 (1993).
15. D. Miyauchi and S. Araki, *Appl. Phys. Lett.* **63,** 1702 (1993).
16. P. Grunberg, R. Schreiber, Y. Pang, M. B. Brodsky, and H. Sowers, *Phys. Rev. Lett.* **57,** 2442 (1986).
17. P. Grunberg, R. Schreiber, Y. Pang, U. Walz, M. B. Brodsky, and H. Sowers, *J. Appl. Phys.* **61**(8), 3750 (1987).
18. A. Barthelemy, A. Fert, M. N. Baibich, S. Hadjoudj, F. Petroff, P. Etienne, R. Cabanel, S. Lequien, F. Nguyen Van Dau, and G. Creuzet, *J. Appl. Phys.* **67,** 5908 (1990).
19 H. Y. Hwang, S.-W. Cheong, N. P. Ong, and B. Batlogg, *Phys. Rev. Lett.* **77,** 2041 (1996). H. Y. Hwang and S.-W. Cheong, *in* "Colossal Magnetoresistance Oxides" (Y. Tokura, Ed.), Monograph in Condensed Matter Science. Gordon and Breach, New York, in press.
20. H. Kuwahara, Y. Tomioka, Y. Moritomo, A. Asamitsu, M. Kasai, R. Kumai, and Y. Tokura, *Science* **272,** 80 (1996).

21. J. Chenavas, J. C. Joubert, M. Marezio, and B. Bochu, *J. Solid State Chem.* **14,** 25 (1975).
22. B. Bochu, J. C. Joubert, A. Collomb, B. Ferrand, and D. Samaras, *J. Magn. Magn. Mater.* **15,** 1319 (1980).
23. M. N. Deschizeaux, J. C. Joubert, A. Vegas, A. Collomb, J. Chenavas, and M. Marezio, *J. Solid State Chem.* **19,** 45 (1976).
24. A. Shainer, M. Croft, Z. Zhang, M. Greenblatt, I. Perez, P. Metcalf, H. Jhans, G. Liang, and Y. Jeon, *Phys. Rev. B* **53,** 9745 (1996).
25. M. Croft, D. Sills, M. Greenblatt, C. Lee, S.-W. Cheong, K. V. Ramanujachary, and D. Tran, *Phys. Rev. B* **55,** 8726 (1997).
26. Z. Tan, S. Heald, S.-W. Cheong, A. Cooper, and A. Moodenbaugh, *Phys. Rev. B* **47,** 12365 (1993).
27. A. Collomb, D. Samaras, J. Chenavas, M. Marezio, J. C. Joubert, B. Bochu, and M. N. Deschizeaux, *J. Magn. Magn. Mater.* **7,** 1 (1978).
28. M. Marezio, P. D. Dernier, J. Chenavas, and J. C. Joubert, *J. Solid State Chem.* **6,** 16 (1973).
29. J. Chenavas, F. Sayetat, A. Collomb, J. C. Joubert, and M. Marezio, *Solid State Commun.* **16,** 1129 (1975).
30. R. D. Shannon, *Acta Crystallogr. A* **32,** 751 (1976).
31. A. H. Morrish, "The Physical Principles of Magnetism," p. 443. Wiley, New York, 1965.
32. For reviews, see: G. Bergmann, *Phys. Rep.* **107,** 1 (1984); P. A. Lee and T. V. Ramakrishnan, *Rev. Mod. Phys.* **57,** 287 (1985); S. Chakravarty and A. Schmid, *Phys. Rep.* **140,** 193 (1986).
33. L. Landau and E. Lifshitz, "Statistical Physics," 3rd edition, Chap. 14. Pergamon Press, New York, 1982.
34. S. Jin, H. M. O'Bryan, T. H. Tiefel, M. McCormack, and W. W. Rhodes, *Appl. Phys. Lett.* **66,** 382 (1995).
35. J. Inou and S. Maekawa, *Phys Rev.* **53B,** 52 (1996).